Check for updates

Aggrandized photocatalytic H$_2$O$_2$ and H$_2$ production by a TiO$_2$/Ti$_3$C$_2$–TiC/mixed metal Ce–Zr MOF composite: an interfacial engineered solid-state-mediator-based Z-scheme heterostructure†

Lijarani Biswal, Suraj Prakash Tripathy, Srabani Dash, Sarmistha Das, Satyabrata Subudhi [ID] and Kulamani Parida [ID] *

The development of well-designed all-solid-state Z-scheme hybrid architectures with highly active distinct functional materials has received huge attention due to their great potential for solar-to-fuel energy production. However, delicately constructing a multiphase heterojunction with a high-flux charge shuttle through material design strategies remains a challenge. Herein, we demonstrate a unique protocol involving a bio-inspired multivariate mediator-based Z-scheme TiO$_2$/Ti$_3$C$_2$–TiC and mixed metal Ce/Zr-UiO-66-NH$_2$ (CZUNH) heterostructure (TiO$_2$/Ti$_3$C$_2$–TiC/CZUNH) by an interfacial engineering approach for highly promoted photocatalytic H$_2$O$_2$ and H$_2$ production. The structural analysis of the TiO$_2$/Ti$_3$C$_2$–TiC/CZUNH composite revealed that CZUNH accumulated on the surface of TiO$_2$/Ti$_3$C$_2$–TiC nanosheets, providing dense active sites for enhanced photocatalytic reactions. The HRTEM and XPS characterization distinctly clarified the close interfacial interaction between CZUNH and TiO$_2$/Ti$_3$C$_2$–TiC. Mechanistic investigation showed that the Ti$_3$C$_2$–TiC nanosheets act as a solid-state electron mediator, constructing an electron-shuttling route between CZUNH and TiO$_2$ and thus extending the lifetime of photo-induced charge carriers generated on CZUNH and TiO$_2$, respectively. Specifically, the transfer channel pathway of the Z-scheme-based TiO$_2$/Ti$_3$C$_2$–TiC/CZUNH-20 composite with a tremendous driving force provides an optimum H$_2$O$_2$ production capacity of 1575 μmol h^{-1} g^{-1}, which is approximately 3.5- and 2.8-fold higher than those of neat TiO$_2$/Ti$_3$C$_2$–TiC and CZUNH, respectively. Moreover, the optimal visible light H$_2$ evolution rate of 570 μmol h^{-1} (with ACE 9.1%) is four and three times higher than those of pristine TiO$_2$/Ti$_3$C$_2$–TiC and CZUNH, respectively. This research provides deep understanding of the design of a highly active mediator-based Z-scheme heterojunction interface for improving the catalytic performance of MXene-derived photocatalysts.

1. Introduction

In recent years, the energy crisis and environmental pollution have become global threats to human society owing to the massive consumption of non-renewable fossil fuels.[1,2] Therefore, scientific communities are seeking for an immutable and sustainable solution to achieve a greener society without any consumption of non-renewable feedstocks. Nowadays,

hydrogen peroxide (H_2O_2) is considered as leading prospective energy transporter for the future owing to its versatile nature, such as eco-friendly, clean, facile storage, easy conveyance, multifunctional oxidation and release of H_2O as a by-product.[3–5] Therefore, it is widely used in the food and paper manufacturing industry, pulp bleaching, medical pasteurization, waste water treatment, organic synthesis and chemical industry with an annual demand of 3 million tons.[6–8] Moreover, H_2O_2 can be restored safely and easily transferred owing to its good water solubility. Currently, H_2O_2 is produced in industry through several techniques, for example, the traditional anthraquinone process, alcohol oxidation, electrochemical fabrication and direct synthesis by mixing H_2 and O_2 gas.[9] Application of these processes is restricted by their elevated temperature, intense energy input, complicated routes, high manufacturing costs and toxic by-products.[10] However, direct preparation of H_2O_2 from H_2 and O_2 through noble metal catalysis is also being intensively investigated, but the usage use of costly rare earth metals and potentially explosive nature of related gases hinder the synthesis process. Therefore, a safe, efficient, environmentally friendly and low-cost method for H_2O_2 production is urgently needed. Recently, photocatalytic H_2O_2 generation from H_2O and O_2 using a sustainable semiconductor-based artificial photocatalyst, whereby the reaction can proceed through several reaction pathways, such as (i) direct single-step (2 e$^-$), (ii) indirect two-step (1 e$^-$) and (iii) addition of two $^{\bullet}$OH radicals, has been receiving extensive attention from the research community.[11–14] However, it is still difficult to achieve large industrial H_2O_2 production using photocatalysts. Additionally, in the era of energy crisis, hydrogen (H_2) has been receiving massive attention as a substitute for non-renewable energy sources due to its clean and sustainable nature. Since the inventive discoveries of Fujishima and Honda, H_2 generation via photocatalytic water splitting over a semiconductor has been recognised as an advantageous strategy for addressing aforementioned concerns.[15] In this regard, various semiconductors have been used for the generation of H_2O_2 and H_2. Among them, TiO_2 is the most promising photocatalyst owing to its appropriate band alignment, strong redox ability, low cost, non-toxicity, and excellent thermal and chemical stability.[16] Nevertheless, the photocatalytic application of TiO_2 is severely restricted by intrinsic shortcomings, such as the wide band gap (3.0–3.2 eV), quick charge recombination, poor visible light harvesting, and low kinetic energy for H_2 production.[17,18] Furthermore, TiO_2 exhibits low efficiency in H_2O_2 production under solar light, which can be attributed to the higher rate of decomposition of adsorbed H_2O_2 on the TiO_2 surface in the form of Ti–OOH complexes by photogenerated holes.[19] Hence, various methods, such as elemental doping, surface modification, loading of a co-catalyst and constructing a heterojunction, have been adopted to promote charge carrier separation for improved photocatalytic applications. However, heterojunction engineering with effective interfacial charge transportation and co-catalyst modification strategies are considered to be particularly promising methods for lowering the recombination rate and improving the lifespan of the photoinduced charge carriers.

In this context, the use of MXene, a transition metal carbide and carbonitride, synthesized by selectively etching the Al layer from the parent precursor MAX phase, has attracted intensive attention for its unique properties, such as metallic conductivity, specific surface area, tuneable surface termination groups, flexible elemental composition and low Fermi level.[20–27] Recently, Ti_3C_2 (titanium carbide), a widely studied MXene, has been used as a robust co-catalyst in photocatalysis, especially when modified with semiconductors such as TiO_2, g-C_3N_4, CdS and $ZnIn_2S_4$, to boost the exciton lifespan and separation efficiency.[28–31] Ti_3C_2 MXene provides a natural Ti source to evolve TiO_2 and establish an atomic-scale interface hybrid structure between TiO_2 and Ti_3C_2 owing to thermodynamically metastable marginal Ti atoms in Ti_3C_2. Moreover, the Ti electron orbitals changed significantly during the slight oxidation process, establishing substantial chemical bonding and ensuring a strong electronic interaction that enhances the transportation and separation of photoinduced excitons.[32] Additionally, metallic $Ti_3C_2T_x$ has the capacity to capture photoexcited electrons, regulating the flow of photogenerated charge carriers. So far, various MXene-derived TiO_2 hybrid structures have been reported with superior spatial separation and transfer of photoinduced charge carriers, including TiO_2/Ti_3C_2/MIS, Cu/TiO_2@$Ti_3C_2T_x$, Ti_3C_2/TiO_2/BiOCl, Ni_2P/TiO_2/Ti_3C_2, Ti_3C_2/TiO_2/ZnCdS and Ru/MXene/TiO_2.[33–39] However, conventional type-II heterojunction photocatalysts display restricted performance because of lower redox potentials needed to produce reactive species during the photocatalytic process.

Owing to above-mentioned aspects, multivariate solid-state Z-scheme heterojunctions, which were influenced by the universal photosynthesis process, have emerged as a substitute to traditional type-II heterojunctions owing to their superior exciton pair segregation and incredible redox ability of the charge carriers. When constructing a Z-scheme heterojunction, the selection of two different types of semiconductor is quite important to couple their energy bands with superior interfacial charge transfer channels. Metal–organic frameworks (MOFs) are porous hybrid crystalline materials with a high specific surface area, tuneable porosity, flexible functionalization and tailorable compositions for the metal centre and organic linker, which makes them exemplar for various applications.[40–42] Unfortunately, pristine MOFs show some inherent drawbacks, such as quick charge recombination, low stability in aqueous conditions and low light-harvesting capacity, which hinder them from becoming robust photocatalysts. To overcome aforementioned issues, numerous mixed metallic MOFs for example UiO-66-NH_2 (Zr-Hf), MIL-125 (Fe–Co), UiO-66 (Ti–Ce) and UiO-66 (Ce–Zr), have been considered.[43–46] Moreover, MOFs containing Ce are considered to be an ideal choice, because of their easy availability and interconvertible flexible Ce^{3+}/Ce^{4+} oxidation state. However, the major drawback of cerium-based MOFs is their low thermal stability and exciton segregation.[47,48] The abovementioned problem can be tackled

by inserting Ce ions into the visible-light-responsive UiO-66 family of Zr-based MOFs, *i.e.*, (Zr) UiO-66-NH$_2$ (ZUNH), in the same aqueous stable framework cluster for enhanced stability and photocatalytic performance.[49] However, ZUNH has some inherent flaws that reduce its effectiveness in several photocatalytic applications, such as rapid exciton recombination, photo-corrosion, and poor stability.[50–53] To overcome these flaws, the construction of heterojunctions has been considered as a remarkable way of enhancing the photocatalytic ability with controlled charge carrier separation. Meanwhile, TiO$_2$ is favourable for constructing multivariate Z-scheme heterostructures because of the wide-ranging bandgap, robust stability, appropriate band structure and effective photocatalytic performance. MXene is a noble-metal-free solid-state electron mediator with superior electrical conductivity and metallic nature, which encourages the construction of an interfacial electron-shuttling path in Z-scheme hybrids. Therefore, multivariate Z-scheme ternary heterostructure exhibit better separation of charge carriers, which boosts the photocatalytic H$_2$O$_2$ and H$_2$ production. However, the construction of ternary Z-scheme hybrids with Ti$_3$C$_2$ MXene as the electron mediator has received very little attention for various photocatalytic applications.

Inspired by above considerations, we explored a novel ternary TiO$_2$/Ti$_3$C$_2$–TiC/CZUNH Z-scheme heterostructure towards visible-light-driven H$_2$O$_2$ and hydrogen production. A two-step oxidation strategy was used to fabricate a unique type of heterojunction, TiO$_2$/Ti$_3$C$_2$–TiC/CZUNH, where metallic Ti$_3$C$_2$ MXene acts as the solid-state electron channelizer to develop an electron-shuttling route between CZUNH and TiO$_2$. A series of analytical techniques were used to explore the structural, morphological, optical and photo-electrochemical properties of the hybrid structure. Furthermore, the mechanism underlying the enhanced photocatalytic performance was explored. The current work provides a blueprint for the design of non-metal-mediator-based Z-scheme heterojunctions for several energy and environmental applications.

2. Experimental section

2.1. Chemicals used

Titanium aluminium carbide MAX phase powder (Ti$_3$AlC$_2$, purity > 98%, ~200 mesh) was procured from Xiamen Tob New Energy Technology. Co. Ltd China. Zirconium chloride (ZrCl$_4$), cerium(III) chloride heptahydrate (CeCl$_3$·7H$_2$O), 2-amino terephthalic acid (ATA), potassium bromide (KBr), Nafion solution, hydrofluoric acid (HF, 40%) and hydrochloric acid (HCl) were purchased from Sigma-Aldrich. Additionally, sodium tetrafluoroborate (NaBF$_4$), methanol (MeOH), sodium sulfate (Na$_2$SO$_4$), and *N,N*-dimethyl formamide (DMF) were procured from Merck. All chemicals were used without any additional purification. Throughout the reaction process, deionized water (DI) was used.

2.2 Preparation of Ti$_3$C$_2$–TiC MXene nanosheets

The Ti$_3$C$_2$T$_x$–TiC nanosheets were synthesized by following the previously reported route *via* etching the Al layer from the Ti$_3$AlC$_2$ MAX phase using HF solution.[54] In this typical synthesis, 1 g of powder Ti$_3$AlC$_2$ was gradually added to 20 mL of HF (40%) solution. Then, the suspension was subjected to stirring at room temperature (RT) for 24 h. After that, the resultant solution was centrifuged many times with DI to reach neutral pH. Then, the obtained slurry was subjected to drying by vacuum oven (50 °C in for 12 h) to obtain multi-layered Ti$_3$C$_2$–TiC nanosheets.
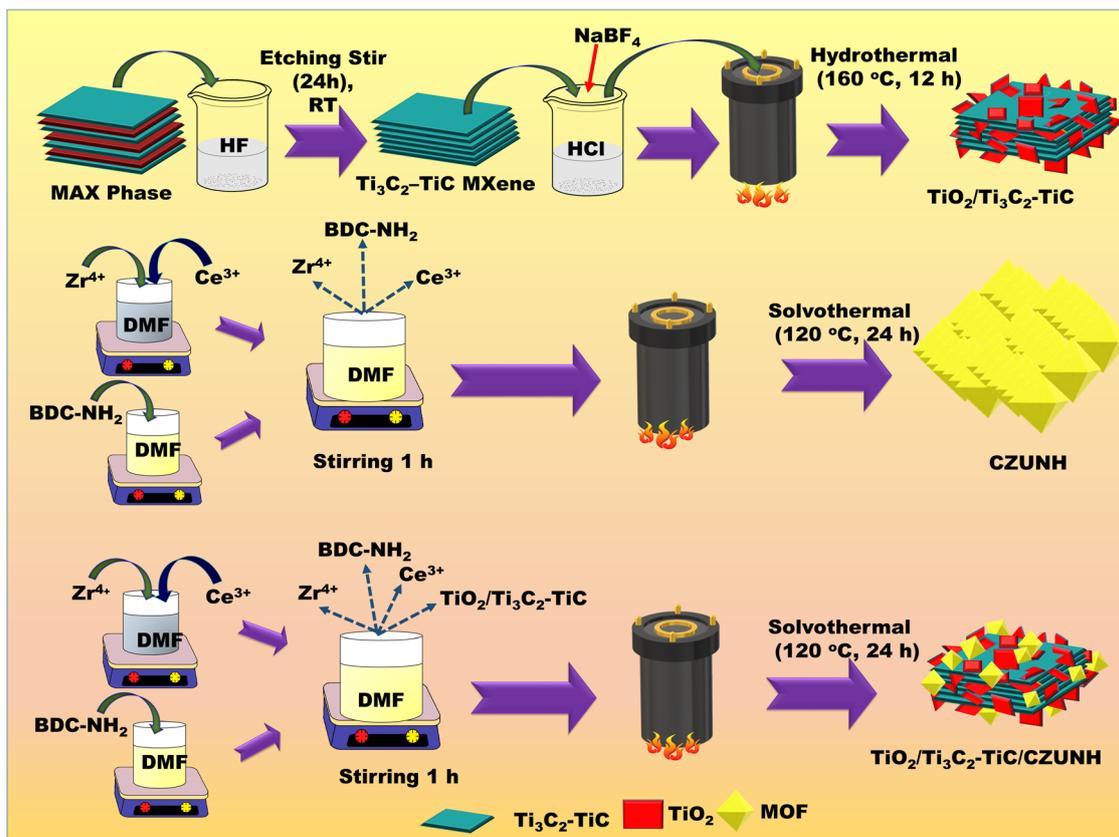
2.3 Preparation of Ti$_3$C$_2$–TiC MXene-derived TiO$_2$

The Ti$_3$C$_2$–TiC derived TiO$_2$ nanohybrid was obtained by a facile hydrothermal approach. Ti$_3$C$_2$–TiC nanosheets (0.1 g) and NaBF$_4$ (0.165 g) were added to 1 M HCl (15 mL) aqueous solution, followed by ultrasonication for 30 min. Then, the dispersed solution was subjected to 30 min of stirring. The resultant solution was transferred into a stainless-steel Teflon-lined autoclave and heated at 160 °C for 12 h. When the reaction was over, the autoclave was cooled down under ambient conditions. Thereafter, the suspension was repeatedly centrifuged with DI and ethanol until decants reached neutral pH. Then, the obtained slurry was dried in a vacuum oven (60 °C, 12 h) (labelled as TiO$_2$/Ti$_3$C$_2$–TiC).

2.4 Preparation of TiO$_2$/Ti$_3$C$_2$–TiC/Mixed metallic CZUNH (Ce/Zr-UiO-66-NH$_2$) nanocomposite (TiO$_2$/Ti$_3$C$_2$–TiC/CZUNH)

The TiO$_2$/Ti$_3$C$_2$–TiC/CZUNH nanocomposite was fabricated *via* a facile solvothermal method by taking certain molar ratios of metal sources ZrCl$_4$ (2.4 mmol) and CeCl$_3$·7H$_2$O (0.6 mmol) and the linker 2-ammino-1,4-benzene dicarboxylic acid (3 mmol). As shown in Scheme 1, the metal salt and linker were dissolved separately in 40 mL of DMF under vigorous stirring for 1 h. Later, resultant suspensions were added together and stirred for 1 h. An adequate amount of pre-synthesized TiO$_2$/Ti$_3$C$_2$–TiC powder was added to the above-mentioned solution through sonication and stirring for 1 h. The obtained suspension was transferred into a Teflon-lined vessel, which was solvothermally heated for 24 h at 120 °C. Thereafter, the autoclave was cooled to room temperature, and the materials were obtained by centrifugation. Subsequently, the pore activation process was carried out with methanol to activate the pores of the MOF composite, followed by drying in a vacuum oven at 70 °C for 24 h. The dried samples were named as TiO$_2$/Ti$_3$C$_2$–TiC/CZUNH-*X*, where *X* is the wt% of CZUNH (10, 20, and 30). Several wt% of TiO$_2$/Ti$_3$C$_2$–TiC/CZUNH nanocomposites (TiO$_2$/Ti$_3$C$_2$–TiC/CZUNH-10, TiO$_2$/Ti$_3$C$_2$–TiC/CZUNH-20, and TiO$_2$/Ti$_3$C$_2$–TiC/CZUNH-30) were synthesized by changing the amount of the precursor CZUNH relative to the fixed TiO$_2$/Ti$_3$C$_2$–TiC content. The bimetallic Ce/Zr-UiO-66-NH$_2$ (CZUNH) was also synthesized using the above mention procedure but without adding TiO$_2$/Ti$_3$C$_2$–TiC. Moreover, in a similar method, monometallic Zr-UiO-66-NH$_2$ (ZUNH) was prepared solvothermally by heating equimolar amounts of ZrCl$_4$ (3 mmol) and the 2-ammino-1,4-benzene dicarboxylic acid linker (3 mmol) at 120 °C for 24 h. Likewise, monometallic Ce-UiO-66-NH$_2$ (CUNH) was prepared by following the same method and heating equimolar amounts of CeCl$_3$·7H$_2$O (3 mmol) and

Scheme 1 Preparation of $Ti_3C_2T_x$–TiC MXene, the TiO_2/Ti_3C_2–TiC nanosheets, and the TiO_2/Ti_3C_2–TiC/CZUNH-X composite.

2-ammino-1,4-benzene dicarboxylic acid linker (3 mmol) at 120 °C for 24 h. The materials prepared were thoroughly characterized, studied and their procedures are discussed in the ESI† section.

3. Results and discussion

3.1 Structural characterization

Phase identification and crystal structure determination of the as-synthesized nanomaterials ($Ti_3C_2T_x$–TiC MXene,

$TiO_2/Ti_3C_2T_x$–TiC, ZUNH, CUNH, CZUNH and TiO_2/Ti_3C_2–TiC/CZUNH-X composites) were carried out using powder X-ray diffraction (PXRD), as shown in Fig. 1(a) and (b). Following HF etching, the intense peak (104) obtained at 39° for Ti_3AlC_2 was completely removed in the etched Ti_3C_2 MXene, which signifies the effective removal of the Al interlayer from the parent precursor MAX phase. Meanwhile, lower angle peaks for the (002) and (004) planes of Ti_3AlC_2 at 9.5° and 19.5°, respectively, broadened due to the formation of the 2D Ti_3C_2 multi-layer and introduction of surface moiety groups (represented
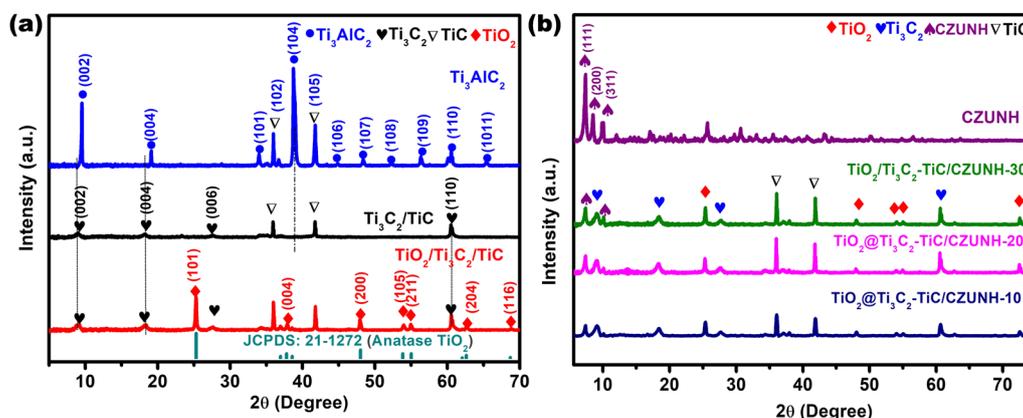

Fig. 1 XRD patterns for (a) Ti_3AlC_2, Ti_3C_2–TiC, TiO_2/Ti_3C_2–TiC, and (b) all of the synthesized TiO_2/Ti_3C_2–TiC/CZUNH-X composites.

by T_x, e.g., –F, –O, and –OH) (Fig. 1(a)).[33] Second, from the XRD analysis, it was also found that low-intensity peaks at around $35°$ and $42°$ are still present in $Ti_3C_2T_x$, which indicates the existence of a small amount of TiC. After the hydrothermal oxidation, the obvious characteristic diffraction peaks of Ti_3C_2 were weaker, while some new strong acicular peaks emerged at $25°$, $37°$, $48°$, $53°$ and $62°$ for the Ti_3C_2/TiO_2 sample, which are associated with the (101), (004), (200), (105) and (206) crystal planes of the anatase phase of TiO_2 (JCPDS no. 21-1271), respectively. This analysis confirms the partial transformation of anatase TiO_2 from the Ti_3C_2–TiC hybrid.[33] Additionally, the CZUNH (Ce/Zr-UiO-66-NH$_2$) bimetallic MOF displays analogous diffraction patterns to those of pristine ZUNH (Zr) and CUNH (Ce) frameworks, which suggests the higher crystallinity and phase purity of the materials (Fig. S1(a)–(c), ESI†). However, the (111) and (200) peaks for CZUNH located at $7.5°$ and $8.5°$ slightly shifted to the lower angle side as compared to pristine ZUNH, which may be ascribed to the integration of Ce ions into the MOF grid by expanding the unit cell with higher lattice parameters (Fig. S1(b), ESI†). The larger ionic radius of the Ce atom (Ce^{3+} = 1.143 and Ce^{4+} = 0.97) in comparison to that of the Zr atom (Zr^{4+} = 0.84) results in larger lattice parameters and expanded unit cell by infiltrating the Zr^{6+} cluster.[55,56] Therefore, decreased in height along with broadening of the XRD peak for CZUNH as compared to that of neat ZUNH suggested the insertion of a Ce atom into the MOF framework lattice and eventually promoted a lowering in Zr-oxy clusters. For the hybrid composite TiO_2/Ti_3C_2–TiC/CZUNH-X, the diffraction peaks assigned to CZUNH are also observed. Interestingly, when the precursor loading amount is increased from 10 to 30 wt%, the intensity of the CZUNH diffraction peak strengthened, and it became dominant, which might be due to the increasing amount of MOF in the nanohybrids (Fig. 1(b)). Furthermore, XRD patterns for ternary hybrid TiO_2/Ti_3C_2–TiC/CZUNH composites easily revealed the existence of the characteristic peaks of anatase TiO_2, Ti_3C_2–TiC and CZUNH, demonstrating the successful synthesis of the ternary hybrid nanostructure.

To reveal different functional groups, chemical composition and bonding structure of the as-prepared samples, Fourier transform infrared (FTIR) spectroscopic analysis was carried out. The related outcomes are illustrated in Fig. S1(c) (ESI†). For TiO_2/Ti_3C_2–TiC, the intense peak at 550 cm^{-1} represents the O–Ti–O vibration, which suggests the partial transformation of anatase TiO_2 from Ti_3C_2. The peaks for the asymmetric and symmetric stretching vibrational modes of amine functional groups in pristine CZUNH were centred at 3475 and 3340 cm^{-1}, respectively. Likewise, the peak at 1245–1640 cm^{-1} was ascribed to the stretching of C–N bond and N–H bending, respectively, due to –NH$_2$ groups present in the linkers.[57] Furthermore, the small peak obtained at around 1510 cm^{-1} represents the vibration of the C=C moiety of the aromatic ring. The vibration peaks at 485, 667 and 760 cm^{-1} were caused by the asymmetric stretching of metal–(OC), bending of O=C=O and stretching of C=C, respectively.[58] The spectra for the TiO_2/Ti_3C_2–TiC/CZUNH composites with different wt%

of MOF contain all the characteristic bands for TiO_2/Ti_3C_2–TiC and CZUNH, signifying an analogous chemical bonding environment and similar functional groups formed in the ternary hybrid framework. This analysis was accordance with previous XRD results.

In addition, Brunauer–Emmett–Teller (BET) and the Barrett–Joyner–Halenda (BJH) analysis were carried out to determine textural features, encompassing surface area and pore volume, of pristine TiO_2/Ti_3C_2–TiC and CZUNH and the TiO_2/Ti_3C_2–TiC/CZUNH-20 composite using the N_2 adsorption–desorption isotherm method (Fig. S2(a)–(c), ESI†). The BET plot of the TiO_2/Ti_3C_2–TiC/CZUNH-20 sample demonstrated a type-IV isotherm with a typical H3 hysteresis loop, demonstrating the mesoporous nature of the hybrid material. In our previous work, the surface area for pristine TiO_2/Ti_3C_2–TiC was found to be 28.3098 m^2 g^{-1}, while on modifying TiO_2/Ti_3C_2–TiC with CZUNH (348.29 m^2 g^{-1}), the BET surface area increased to 72.054 m^2 g^{-1}.[33] In brief, the increased BET surface area of the TiO_2/Ti_3C_2–TiC/CZUNH-20 composite showed a highly active surface, which is an important factor in the enhanced photocatalytic performance.

The surface chemical composition and elemental valence state in the fabricated samples were investigated by X-ray photoelectron spectra (XPS). The full-scale XPS survey spectra of the TiO_2/Ti_3C_2–TiC/CZUNH hybrid presented in Fig. S3(a) (ESI†) revealed that Ti, C, O, Ce, Zr, and N are predominant elements, which suggests that TiO_2, Ti_3C_2 and CZUNH are present in the TiO_2/Ti_3C_2–TiC/CZUNH nanocomposite. The survey result coincides with the elemental mapping and EDX outcomes. Meanwhile, it should be noted that F$^-$ ions that are physically decorated on the MXene surface during the etching process are quite discernible.[33] Moreover, during the two-step hydrothermal process the intensity of the peak for F element was decreased in the ternary hybrid due to the substitution of the –F terminal group by the –O terminal group. The high-resolution XPS spectrum of Ti 2p is deconvoluted into four peaks as illustrated in Fig. 2(a). Among them, two strong peaks situated at binding energies (BE) of 459.1 eV (Ti 2p$_{3/2}$) and 464.9 eV (Ti 2p$_{1/2}$) correspond to the Ti-O lattice in TiO_2. Meanwhile, another two peaks located at BE of 454.8 eV (Ti 2p$_{3/2}$) and 461 eV (Ti 2p$_{1/2}$) are ascribed to the Ti–C lattice in Ti_3C_2–TiC. In addition, deconvoluted peaks at 455.6 and 462.2 eV are attributed to Ti-X from titanium oxycarbides or substoichiometric TiC$_x$ (X < 1). The peaks at 456.9 and 463.5 eV could result from Ti_xO_y (Ti species with a reduced charge state).[33] Besides, the BE of Ti in the TiO_2/Ti_3C_2–TiC/CZUNH hybrid revealed a prominent negative shift toward lower BE as compared with TiO_2/Ti_3C_2–TiC, which also ensures sufficient contact between phases and guarantees the electron flow between ternary composites after loading CZUNH. In addition, Fig. S3(b) (ESI†) shows that the higher resolution C1s spectra of TiO_2/Ti_3C_2–TiC, and the TiO_2/Ti_3C_2–TiC/CZUNH composite was deconvoluted into five characteristic peaks. The peak at 284.8 eV is ascribed to C–C coordination, attributed to the surface adventitious carbon. Other peaks located at 281.4, 283.6, 286.4, 286.6 and 288.5 eV correspond to C–Ti, C–Ti–Oa
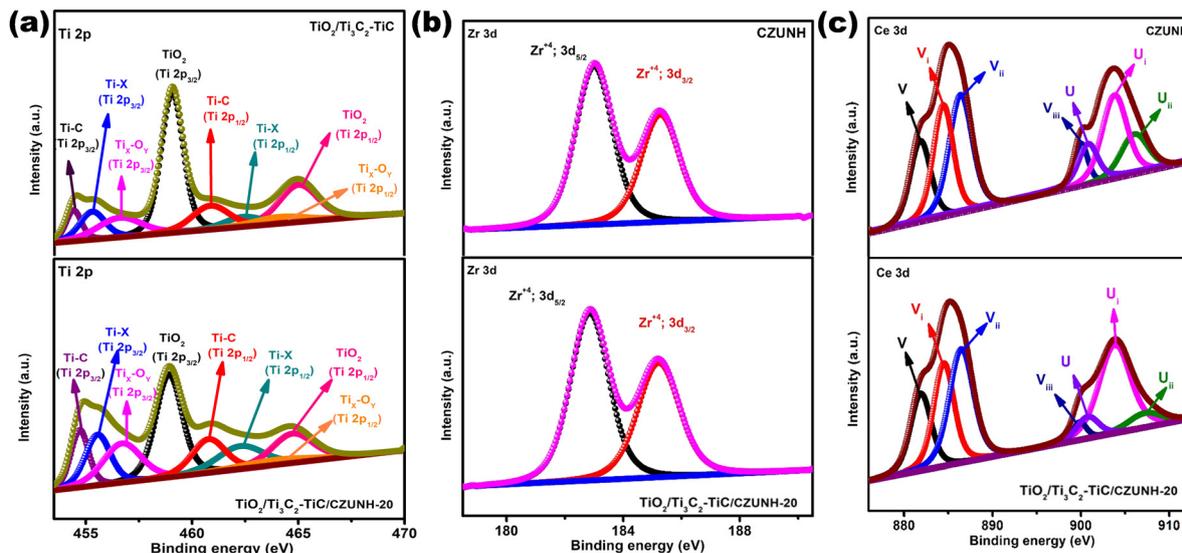
Fig. 2 XPS spectra of (a) Ti 2p, (b) Zr 3d and (c) Ce 3d for TiO$_2$/Ti$_3$C$_2$–TiC, CZUNH and the TiO$_2$/Ti$_3$C$_2$–TiC/CZUNH-20 composite, respectively.

(which denotes the –OH termination group on the Ti$_3$C$_2$ surface), C–O, C–NH$_2$ and –O–C=O/C–F, respectively.[33,52] Additionally, it was noticed that the peak of the C–Ti bond in the TiO$_2$/Ti$_3$C$_2$–TiC/CZUNH composite is significantly lower intensity as compared to that of pristine TiO$_2$/Ti$_3$C$_2$–TiC, indicating the substitution of C–Ti into the Ti–O bond after applying the hydrothermal approach. The peak for the C–Ti bond in the TiO$_2$/Ti$_3$C$_2$–TiC/CZUNH ternary hybrid showed a slight negative shifting (0.1 eV), signifying the transfer of electrons in the heterojunction. The O 1s XPS spectrum is exhibited in Fig. S3(c) (ESI†). The peaks attributed to –OH, Zr–O, Ti–OH, C–Ti–O, O–lattice and Ti–O–Ti bonds are located at binding energies of 532.9, 532.3 531.7, 531.1, 530.1 and 529.5 eV, respectively. Further, this analysis not only endorses the formation of TiO$_2$ but also signifies the oxygen functionalization of MXene during the two-step oxidation process. Fig. 2(b), (c) and Fig. S3(d) (ESI†) show high-resolution Zr 3d, Ce 3d and N 1s XPS spectra for neat CZUNH and the TiO$_2$/Ti$_3$C$_2$–TiC/CZUNH composite. The Zr spectra show two peaks at 182.8 and 185.2 eV, which are allocated to Zr 3d$_{5/2}$ and Zr 3d$_{3/2}$ spin states, respectively.[52] The XPS spectra for Ce contain two sets of peaks representing Ce 3d$_{5/2}$ (as V) and Ce 3d$_{3/2}$ (as U) states. The peaks labelled with V (excluding Vi) and U (excluding Ui) correspond to the Ce ion in the 4+ oxidation state, while the peaks labelled Vi and Ui represent the Ce ion in the 3+ oxidation state. From the above analysis, Ce ions existed in 3+ and 4+ oxidation states in the framework, signifying the construction of a mixed-valence MOF.[59] From Fig. S3(d) (ESI†), the N 1s XPS spectrum shows characteristic peaks at 399.3 and 400.03 eV for the amine functional groups of the linkers (–NH$_2$ and –NH$_3^+$).[52] Summarily, the XPS spectra comprehensively reveal the role of the Ce^{3+}/Ce^{4+} redox pair and prove the successful construction of the bimetallic single component MOF in the TiO$_2$/Ti$_3$C$_2$–TiC/CZUNH ternary hybrid. In comparison to pristine CZUNH, Zr 3d, Ce 3d, and N 1s peaks for the TiO$_2$/Ti$_3$C$_2$–TiC/CZUNH-20 composite are slightly shifted toward higher binding energies, indicating variations in the electron densities of the distinct materials in the TiO$_2$/Ti$_3$C$_2$–TiC/CZUNH-20 composite owing to the migration of electrons from the CZUNH to TiO$_2$ via the Ti$_3$C$_2$ charge mediator. Typically, photogenerated electrons from n-type CZUNH are transferred to n-type TiO$_2$, induced an increase in the electron density on the TiO$_2$ surface, causing the binding energy to shift towards a lower value (redshift). In addition, the increased binding energy (blue shift) was guaranteed by the decrease in the electron density on the CZUNH surface. The aforementioned result indicates a shift in the BE of the core level electrons of these ions, verifying the presence of a reasonably strong interaction between CZUNH and TiO$_2$/Ti$_3$C$_2$–TiC. It also provides evidence of the establishment of a mediator-induced Z-scheme heterojunction.

3.2 Morphological characterization

The morphological structures of the TiO$_2$/Ti$_3$C$_2$–TiC/CZUNH (Ce/Zr) nanocomposite were analysed by FESEM and HRTEM. As shown in Fig. 3(a), Ti$_3$C$_2$ exhibited an accordion-like morphology with a smooth surface texture, demonstrating the effective removal of the Al layer from the Ti$_3$AlC$_2$ layer.[32] As a result, a typical MXene morphology was formed after the etching process. This accordion interconnected layer structure provides abundant specific active sites and surface area, which is advantageous for creating a huge platform for constructing an efficient photocatalytic-based heterojunction. After in situ hydrothermal treatment of Ti$_3$C$_2$ MXene in the presence of a structure-directing agent (NaBF$_4$), TiO$_2$ nanosheets were inserted across the layered Ti$_3$C$_2$ nanosheets owing to the metastable thermodynamic state of the marginal Ti atoms in the accordion layer of MXene (Fig. 3(b)). Meanwhile, –F terminations were replaced by –O and –OH in the aqueous acidic environment, and the TiO$_2$ nanosheets were created as by-products owing to the defects of Ti$_3$C$_2$, resulting in the
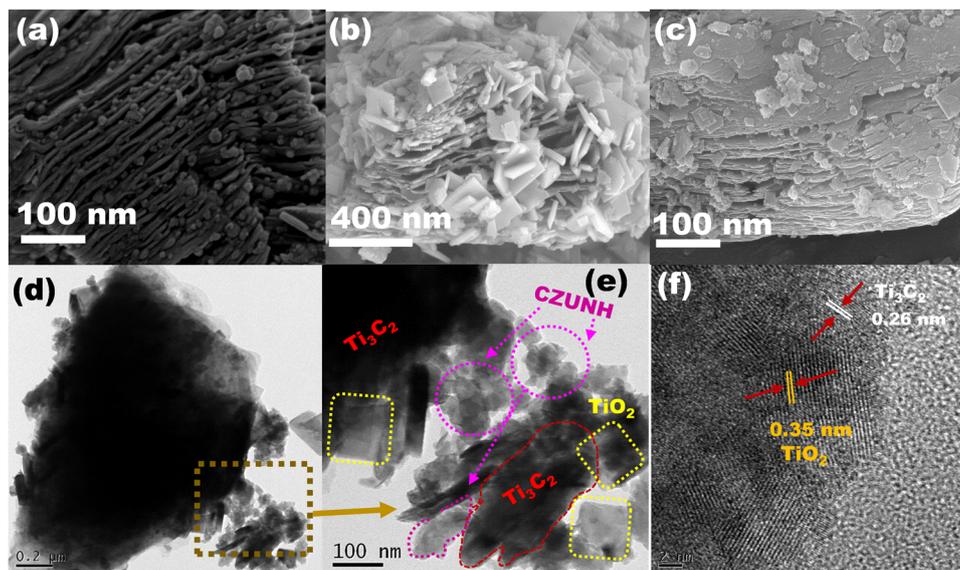
Fig. 3 FESEM images of (a) Ti_3C_2–TiC, (b) TiO_2/Ti_3C_2–TiC and (c) the TiO_2/Ti_3C_2–TiC/CZUNH-20 composite. (d)–(f) HRTEM images of the TiO_2/Ti_3C_2–TiC/CZUNH-20 composite.

construction of a well-designed 2D–2D TiO_2/Ti_3C_2–TiC heterostructure. Fig. 3(c) shows an FESEM image of the TiO_2/Ti_3C_2–TiC/CZUNH-20 (Ce/Zr) composite photocatalyst, in which CZUNH bimetallic MOF nanoparticles are decorated on the surface of the TiO_2/Ti_3C_2–TiC heterostructure, promoting a close interfacial heterostructure between the CZUNH bimetallic MOF and TiO_2/Ti_3C_2–TiC, which may improve the photoexcited charge diffusion under illumination of visible light. Moreover, HRTEM analysis was employed to elucidate the morphology and microscopic structure of the TiO_2/Ti_3C_2–TiC/CZUNH composites. Fig. S4(a) (ESI†) shows that the TiO_2 nanosheets were grown *in situ* at the edge of Ti_3C_2. The corresponding HRTEM image (Fig. S4(b), ESI†) of CZUNH shows the granular nanoparticle-like morphology. Fig. 3(d)–(f) show typical HRTEM images of TiO_2/Ti_3C_2–TiC and the CZUNH bimetallic MOF composite. The TiO_2 nanosheets were evenly grown across the Ti_3C_2–TiC layer owing to the titanium atoms of Ti_3C_2 being transformed into hydrated Ti^{3+} ions under an acidic hydrothermal environment and being prone to oxidation, resulting in TiO_2 at the defect sites of Ti_3C_2–TiC, demonstrating a robust 2D/2D hybrid nanostructure consisting of the TiO_2 nanosheets and Ti_3C_2–TiC nanosheets. From Fig. 3(e), it is evident that in TiO_2/Ti_3C_2–TiC/CZUNH, the bimetallic MOF nanoparticles are accumulated on the TiO_2/Ti_3C_2–TiC nanosheets to form intimate hybridized TiO_2/Ti_3C_2–TiC/CZUNH triple hybrids, which is corroborated by the FESEM image. Moreover, lattice spacings given in Fig. 3(f) of 0.35 nm and 0.26 nm were assigned to the (101) plane of anatase TiO_2 and the (010) plane of Ti_3C_2.[33] However, the lattice spacing of bimetallic CZUNH is absent owing to its electron-sensitive nature. The SAED pattern of the TiO_2/Ti_3C_2–TiC/CZUNH composite depicted in Fig. S4(c) (ESI†) reveals the existence of the TiO_2, Ti_3C_2 and bimetallic MOF in the ternary hybrid, as previously reported.[32,33] The EDX and colour elemental mappings of the composite in Fig. S4(d)–(k)

and Fig. S5 (ESI†) reveal the homologous arrangement of Ti, C, Zr, Ce, O and N elements within a certain area, confirming the generation of the TiO_2/Ti_3C_2–TiC/CZUNH hybrid. Furthermore, the results of the FESEM and HRTEM analyses aid in visualizing and demonstrating the formation of the ternary composite. As a result, a close interfacial well-designed heterojunction was observed, which would be favourable for faster charge carrier transfer and separation efficiency. The analysis is in good accordance with the XPS survey spectrum. Hence, all above-mentioned results firmly evidence the construction of a unique well-designed ternary heterojunction by a two-step hydrothermal process, which ensures sufficient contact between parent material phases for efficient charge carrier transfer and separation.

3.3 Optical characterization

UV-Vis diffuse reflectance spectroscopy (UV-vis DRS) was applied to investigate the optical absorption and band structure of the prepared photocatalysts (Fig. 4(a)). Therein, Ti_3C_2–TiC MXene displays a strong characteristic absorption spectrum in the entire 250–800 nm region, which is attributed to its dark colour and metallic conductivity.[32,33] Moreover, the TiO_2/Ti_3C_2–TiC composite shows a distinct absorption band edge, which represents the *in situ* growth of TiO_2 after the hydrothermal treatment of Ti_3C_2. The pristine bimetallic CZUNH exhibits two strong bands. The acute band at 265 nm represents the n–π* transition for the lone pair of electrons in the –NH_2 group of the ATA linker. Meanwhile, the absorption band at 365 nm indicates the overlapping of the π–π* transitions of the linker with those of the Zr-oxy cluster.[52,60–62] Further, the TiO_2/Ti_3C_2–TiC/CZUNH hybrid exhibited a substantial red shift in the absorption edge, and the improved absorption in the visible region was attributed to the optical absorption of the Ti_3C_2 and CZUNH components. From Tauc plots, the optical band gap
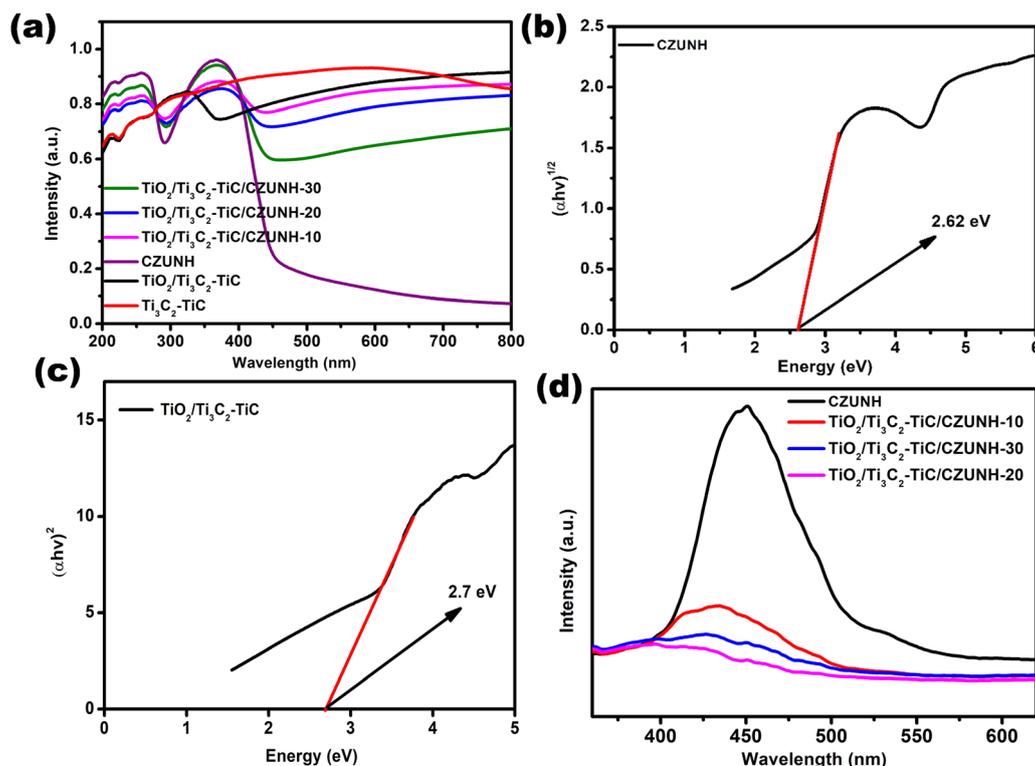
Fig. 4 (a) UV-vis DRS spectra of all the synthesized materials. Energy band gaps of (b) CZUNH and (c) TiO_2/Ti_3C_2–TiC. (d) Photoluminescence spectra of all the fabricated materials.

energy of TiO_2/Ti_3C_2–TiC and bare bimetallic CZUNH were calculated using the Kubelka–Munk equation:

$$\alpha h\nu = A(h\nu - E_g)^{n/2} \qquad (1)$$

Here, α is the absorption coefficient, ν and h signify the light frequency and Planck constant, respectively, E_g represents the band gap energy, A signifies the proportionality constant and n shows the electronic transition of the photocatalysts. As shown in Fig. 4(b) and (c), the band gaps of TiO_2/Ti_3C_2–TiC and CZUNH were evaluated to be 2.7 eV and 2.62 eV, respectively.

To ascertain the lifespan of the photoinduced charge carriers, steady-state luminescence analysis was carried out. This provides a comprehensive pathway for the movement and recombination of exciton pairs caused by the inter-electron mechanism on the surface and at the interface of semiconductor-based photocatalytic materials. A small luminescence intensity denotes a lower charge carrier recombination, and a high luminescence intensity indicates greater recombination of the photo-excited charge carriers. The outcomes are shown in Fig. 4(d); owing to the rapid recombination rate of photogenerated excitons, neat TiO_2/Ti_3C_2–TiC and CZUNH displayed higher PL emission intensities than that of the composite. Moreover, the PL peak intensity of the TiO_2/Ti_3C_2–TiC/CZUNH hybrid was significantly lower than those of pristine materials, indicating a strong phase interaction that significantly enhances the charge carrier segregation and migration through a Z-scheme mechanism in which Ti_3C_2–TiC acts as a solid-state electron mediator. Among all the

fabricated samples, the intensity of the TiO_2/Ti_3C_2–TiC/CZUNH-20 composite is the lowest, resulting in superior photo-induced charge carrier separation and movement by inhibiting the recombining process of e^-/h^+ pairs and thus providing higher photocatalytic activity. Time-resolved photoluminescence (TRPL) spectroscopic analysis was also carried out to define the charge transfer dynamics of the TiO_2/Ti_3C_2–TiC/CZUNH-20 sample. As illustrated in Fig. S6 (ESI†) the decay curve of TiO_2/Ti_3C_2–TiC/CZUNH-20 is fitted. The average lifespan of the ternary TiO_2/Ti_3C_2–TiC/CZUNH-20 nanocomposite is 1.17 ns, which is lower than that of pristine TiO_2/Ti_3C_2–TiC (1.32 ns) as reported previously.[33] This finding suggests that the addition of Ti_3C_2–TiC MXene facilitates the enhanced charge carrier separation and transfer pathway of the Z-scheme mechanism.

3.4 Electrochemical characterization

Electrochemical impedance analysis was carried out to enhance comprehension of the efficient photogenerated charge separation occurring in the Z-scheme mediator-based samples. EIS data can be used to interpret the separation and migration of the photogenerated charge carriers at semiconductor and electrolyte interfaces from the interfacial reaction capability. The semicircle arc and straight line obtained in high and low frequency regions are related to the photocatalytic activity of the fabricated samples. The EIS performance of pristine TiO_2/Ti_3C_2–TiC, CZUNH and the TiO_2/Ti_3C_2–TiC/CZUNH-20 hybrid have been depicted in Fig. 5(a). From the Nyquist plot, it can be
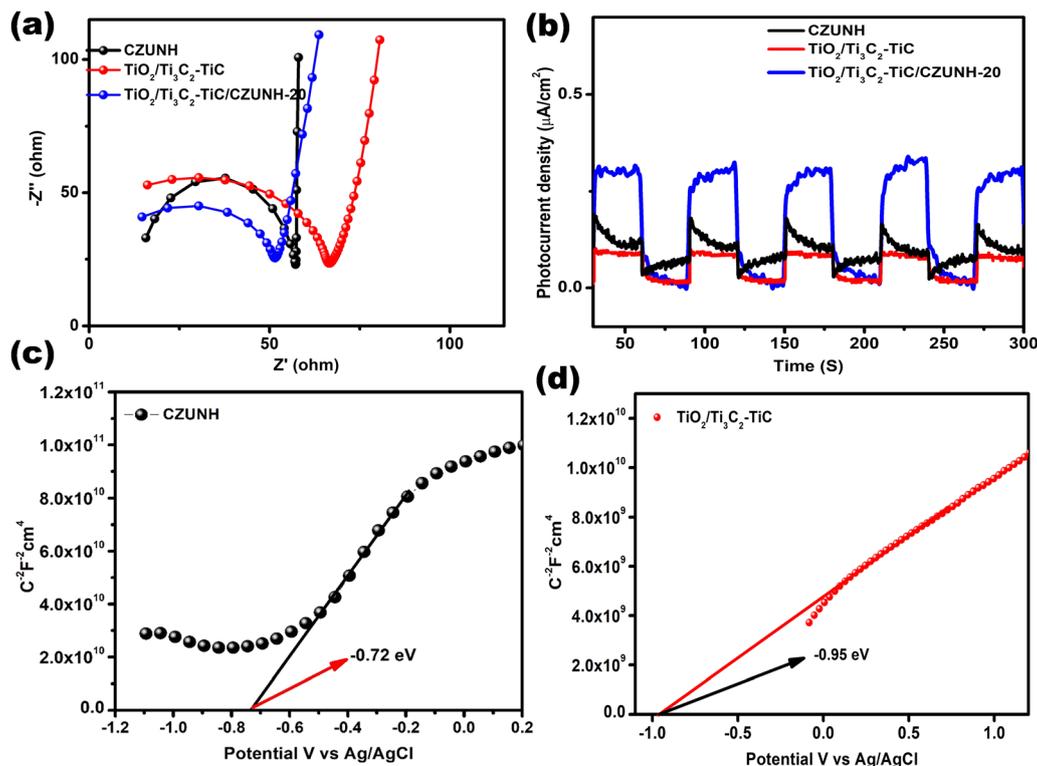
Fig. 5 (a) EIS analysis plot and (b) transient photocurrent for CZUNH, TiO$_2$/Ti$_3$C$_2$–TiC and the TiO$_2$/Ti$_3$C$_2$–TiC/CZUNH-20 composite. Mott–Schottky analysis for (c) CZUNH and (d) TiO$_2$/Ti$_3$C$_2$–TiC.

clearly seen that after modifying TiO$_2$/Ti$_3$C$_2$–TiC with CZUNH, the resulting TiO$_2$/Ti$_3$C$_2$–TiC/CZUNH-20 hybrid exhibits a reduced arc radius and diminished vertical line as compared to the pristine materials, which indicates the presence of a tight interfacial junction between TiO$_2$/Ti$_3$C$_2$–TiC and CZUNH and enhanced charge carrier transfer across the heterojunction.[63–65] Hence, the EIS analysis of the TiO$_2$/Ti$_3$C$_2$–TiC/CZUNH-20 hybrid confirmed the reduced charge transfer resistance, enhanced charge flux and higher electrical conductivity at the electrode–electrolyte interface and hence the increased charge shuttling.

The transient photocurrent response was also measured to further elucidate the charge transfer properties of representative pristine TiO$_2$/Ti$_3$C$_2$–TiC, CZUNH and the TiO$_2$/Ti$_3$C$_2$–TiC/CZUNH-20 hybrid. The current–time curve was plotted for a certain 30 s light on/off cycle (Fig. 5(b)). The photocurrent density of the sample suddenly increases owing to the non-faradaic current during the supply of light. The current density of the TiO$_2$/Ti$_3$C$_2$–TiC/CZUNH-20 hybrid is higher than that of pristine TiO$_2$/Ti$_3$C$_2$–TiC and CZUNH, suggesting the higher efficiency of photogenerated charge separation when using the TiO$_2$/Ti$_3$C$_2$–TiC/CZUNH-20 hybrid structure. Additionally, the built heterojunction having a strong interfacial contact is the major reason for the spatial charge carrier recombination and higher photocatalytic activity.

To further support the superior photoelectrochemical performance of the as-prepared electrodes, a Mott–Schottky (MS) study was performed to describe the band potential and nature

of the mediator-based Z-scheme photocatalysts. The Mott–Schottky plots for TiO$_2$/Ti$_3$C$_2$–TiC and CZUNH are shown in Fig. 5(c) and (d); all samples exhibit a positive slope, signifying n-type characteristics. The values for the flat-band potential (E_{fb}) were obtained by extending the space charge capacitance (C^{-2}) value to zero. The E_{fb} values for TiO$_2$/Ti$_3$C$_2$–TiC and CZUNH were estimated to be −0.95 eV and −0.72 vs. Ag/AgCl, respectively. Again, according to our previous article, the obtained E_{fb} vs. Ag/AgCl were converted to the normal hydrogen electrode (NHE) scale by applying the Nernst equation. Generally, in n-type semiconductors, the CB of the semiconductor positioned approximately 0.1–0.2 eV away from their flat-band potential value on the NHE scale. As a result, the CB of TiO$_2$/Ti$_3$C$_2$–TiC and CZUNH were determined to be −0.46 and −0.24 eV versus NHE, respectively. The following equation was used to calculate the VB of TiO$_2$/Ti$_3$C$_2$–TiC and CZUNH.

$$E_{CB} = E_{VB} - E_g \qquad (2)$$

Here, E_g refers to the band gap energy of the semiconductor (obtained from UV-vis DRS analysis). The E_{VB} of TiO$_2$/Ti$_3$C$_2$–TiC and CZUNH were estimated to be 2.24 and 2.38 eV, respectively.

4. Photocatalytic activity study

The catalytic activity of the fabricated photocatalysts toward H$_2$O$_2$ and H$_2$ production under visible light irradiation was thoroughly investigated.

4.1 Photocatalytic H$_2$O$_2$ production

Photocatalytic H$_2$O$_2$ generation is a green and promising O$_2$ reduction approach using renewable solar energy and Earth-rich O$_2$ as the reaction feedstock. A reaction model experiment was conducted to estimate the catalytic efficacy of the fabricated TiO$_2$/Ti$_3$C$_2$–TiC and CZUNH composites. Fundamentally, two processes, *i.e.*, (i) a direct two-electron reduction procedure carried out by the reduction of dissolved oxygen and (ii) an indirect one-electron reduction process is involved in the oxidation of alcohol (i-PA) and the creation of the superoxide radical in the presence of photoinduced h$^+$, which produces protons during the photoreduction of O$_2$ to H$_2$O$_2$. Moreover, the CB band edge potential of the photocatalyst should be E^0 = −0.33 V *vs.* NHE for the single-electron two-step reduction process and E^0 = +0.68 V *vs.* NHE for the two-electron single-step oxygen reduction reaction (ORR), *i.e.*, generation of H$_2$O$_2$ from dissolved O$_2$. The photocatalytic H$_2$O$_2$ production ability of the synthesized samples was evaluated in an O$_2$-saturated atmosphere under visible light illumination for 1 hour. As shown in Fig. 6(a) and (b), pristine ZUNH, CZUNH and TiO$_2$/Ti$_3$C$_2$–TiC generated very low amounts of H$_2$O$_2$ at 402, 546, and 450 μmol h^{-1} g^{-1}, respectively; this could be attributed to the lower amount of light absorption and rapid charge segregation of the photoinduced excitons. Moreover, after the modification of CZUNH with TiO$_2$/Ti$_3$C$_2$–TiC, the TiO$_2$/Ti$_3$C$_2$–TiC/CZUNH composite showed higher H$_2$O$_2$ production due to the

Z-scheme charge transfer mechansim where metallic MXene acts as a mediator between TiO$_2$ nanosheets and CZUNH framework. Interestingly, the maximum H$_2$O$_2$ generation with TiO$_2$/Ti$_3$C$_2$–TiC/CZUNH-20 was 1575 μmol h^{-1} g^{-1}, which is 3.9, 2.8 and 3.5 times higher than those of bare ZUNH, CZUNH and TiO$_2$/Ti$_3$C$_2$–TiC, respectively. The improved photocatalytic activity can be ascribed to the effective and superior charge carrier separation through the mediator-based Z-scheme charge dynamic. However, on increasing the content of CZUNH in the hybrid TiO$_2$/Ti$_3$C$_2$–TiC/CZUNH-30 composite, the activity yield showed a declining trend, which was attributed to the light-shielding effects of CZUNH blocking the light from reaching TiO$_2$. To determine the reactive species responsible for the production of H$_2$O$_2$, a scavenger test was performed over the TiO$_2$/Ti$_3$C$_2$–TiC/CZUNH composite, and the results are presented in Fig. S7 (ESI†). The scavenging reagents *para*-benzoquinone (*p*-BQ), isopropanol (IPA), citric acid (CA) and dimethyl sulfoxide (DMSO) were used to investigate the role of the active species $^\bullet$O$_2^-$, $^\bullet$OH, h$^+$ and e$^-$, respectively, during the H$_2$O$_2$ production. Based on the results, it can be determined that the superoxide radical anion $^\bullet$O$_2^-$ and e$^-$ play major roles in the formation of H$_2$O$_2$ *via* indirect and direct O$_2$ reduction pathways. Furthermore, the addition of CA and IPA slightly slowed down the H$_2$O$_2$ yield, indicating that h$^+$ and $^\bullet$OH radicals may have minor roles as reactive intermediate species in the photocatalytic H$_2$O$_2$ production process. Since it is well-
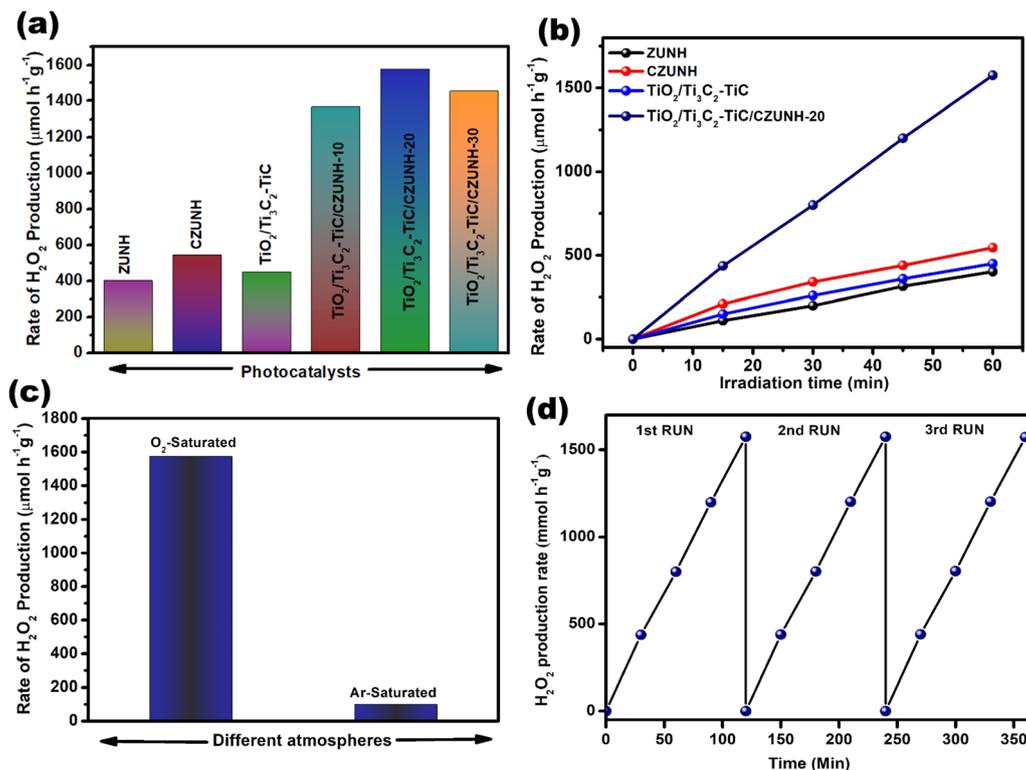

Fig. 6 (a) Bar diagram of H$_2$O$_2$ production by the as-synthesized ZUNH, CZUNH, TiO$_2$/Ti$_3$C$_2$–TiC and TiO$_2$/Ti$_3$C$_2$–TiC/CZUNH-*X* ternary photocatalysts after 2 h illumination. (b) H$_2$O$_2$ generation at different time intervals. (c) Comparison of H$_2$O$_2$ production under different environments. (d) Reusability test for the TiO$_2$/Ti$_3$C$_2$–TiC/CZUNH-20 photocatalyst.

known that photocatalytic H_2O_2 generation is an O_2 reduction reaction, the O_2-saturated environment was regarded as a key factor. Experiments on the generation of H_2O_2 in Ar- and O_2-environments saturated were also carried out to ascertain the importance of O_2. Fig. 6(c) shows that only a very small amount of H_2O_2 was generated in the Ar-saturated environment as compared to the O_2-saturated atmosphere. This finding signified that environmental conditions have a significant impact on the photocatalytic H_2O_2 production and that dissolved O_2 has a significant role in this photocatalytic reaction. Fig. 6(d) clearly shows that the H_2O_2 production rate of the photocatalyst was stable for three consecutive photocatalytic reaction cycles, with a negligible reduction in the photocatalytic performance, suggesting the higher structural stability and durability of the ternary hybrid. This demonstrated the excellent structural photostability efficiency of the ternary hybrid. Moreover, the enhanced H_2O_2 production of the current photocatalytic system is compared with other reported systems in Table S1 (ESI†).

4.2 Photocatalytic H_2 evolution

After investigating the H_2O_2 production, the photon-mediated H_2 evolution performance of the prepared samples (pristine ZUNH, CZUNH, TiO_2/Ti_3C_2–TiC, and TiO_2/Ti_3C_2–TiC/CZUNH) was analysed under visible light illumination, using methanol as a sacrificial agent (hole scavenger), as illustrated in Fig. 7(a).

The generation of hydrogen increased steadily with irradiation time for all the samples (Fig. 7(b)). The photocatalytic activity of the neat ZUNH, CZUNH and TiO_2/Ti_3C_2–TiC is low, which may be attributed to their low light absorption ability and a higher rate of recombination of the photoexcited charge carriers. As compared to the neat counterparts, the TiO_2/Ti_3C_2–TiC/CZUNH composite shows significantly higher photocatalytic H_2 evolution, suggesting the synergistic effect between the Ti_3C_2–TiC nanosheets as a metallic electron mediator, the TiO_2 nanosheets, and the CZUNH framework. The trend in the H_2 evolution rate of the different wt% CZUNH loading TiO_2/Ti_3C_2–TiC composites is in the order of TiO_2/Ti_3C_2–TiC/CZUNH-10 < TiO_2/Ti_3C_2–TiC/CZUNH-30 < TiO_2/Ti_3C_2–TiC/CZUNH-20. From the above analysis, the photocatalytic rate first increased and further decreased with the increased loading of CZUNH because some part of CZUNH can hinder the absorption of incident light and generation of the photoexcited charge carriers by TiO_2. In addition, excessive CZUNH could act as a new recombination centre for the charge carriers. Notably, the TiO_2/Ti_3C_2–TiC/CZUNH-20 composite possesses the best H_2 evolution rate *i.e.*, 570 µmol h^{-1}, which is nearly three and four times higher than the rates obtained for pristine CZUNH and TiO_2/Ti_3C_2–TiC. In addition, the stability of the photocatalysts for the hydrogen evolution reaction was investigated by performing a recycling study (Fig. 7(c)). The enhanced photocatalytic H_2 evolution rate of the TiO_2/Ti_3C_2–TiC/CZUNH-20 composite

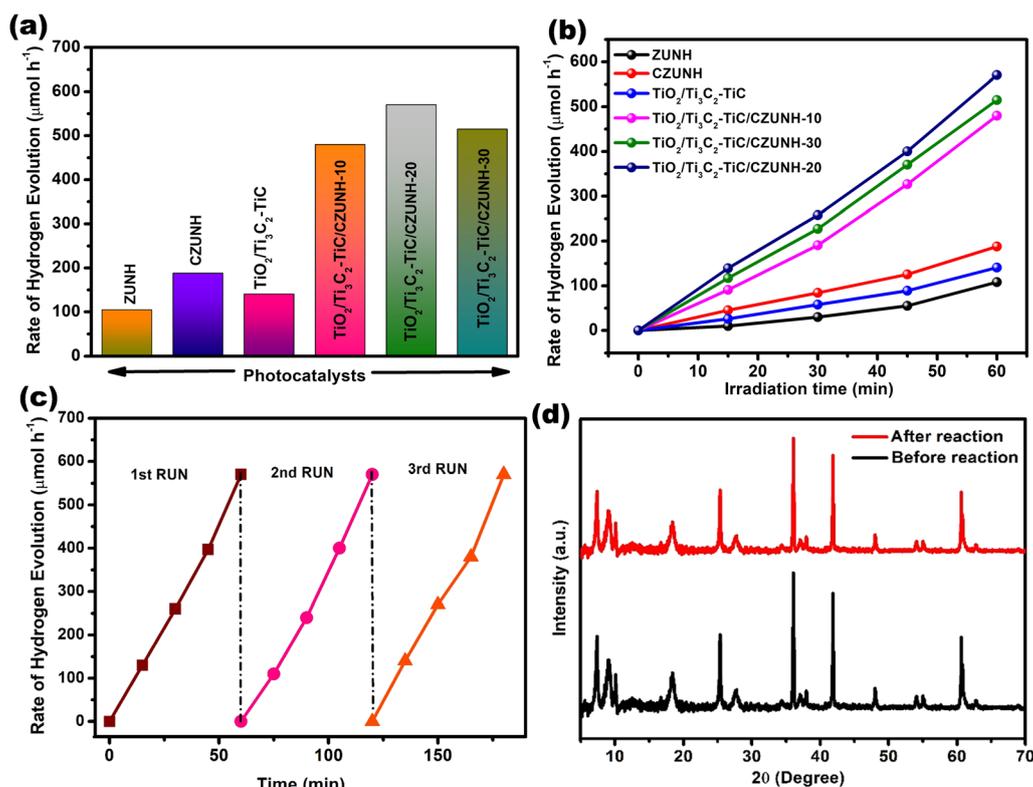**Fig. 7** (a) Photocatalytic H_2 production rate over all the synthesized samples. (b) H_2 evolution for the ZUNH, CZUNH, TiO_2/Ti_3C_2–TiC and TiO_2/Ti_3C_2–TiC/CZUNH-*X* ternary photocatalysts at regular time intervals. (c) Recycling test for the TiO_2/Ti_3C_2–TiC/CZUNH-20 composite for H_2 evolution. (d) XRD pattern for the TiO_2/Ti_3C_2–TiC/CZUNH-20 composite before and after the reaction.

showed no notable variation after three consecutive cycles under visible light irradiation, suggesting the superior stability and robustness of the ternary hybrid towards its practical application. Meanwhile, the extraordinary physicochemical stability of the composite was characterized by PXRD, and no significant changes occurred after performing the photocatalytic reaction, which clearly demonstrates the superior structural photostability of the ternary hybrid (Fig. 7(d)). The apparent H_2 conversion efficiency by the TiO_2/Ti_3C_2–TiC/CZUNH composite was found to be 9.1%. Table S2 (ESI†) presents a comparison of the advanced photocatalytic H_2 evolution activity of the TiO_2/Ti_3C_2–TiC/CZUNH heterojunction with recently reported results for MXene-derived systems.

4.3 Mechanistic insights

Based on the aforementioned physicochemical characterization and photocatalytic study, the possible mechanistic pathway for the synthesized photocatalyst TiO_2/Ti_3C_2–TiC/CZUNH toward visible-light-driven H_2O_2 and H_2 production was elucidated, as depicted in Scheme 2. By combining the UV-vis DRS and Mott–Schottky analysis, the CB for neat TiO_2/Ti_3C_2–TiC and CZUNH were calculated to be -0.46 and -0.24 eV, respectively, and their VB were determined to be 2.2 and 2.38 eV ($vs.$ NHE), respectively. Owing to higher metallic characteristics, MXene

possesses higher electron mobility and acts as the channelizer to promote spatial charge separation. To establish the proposed mechanism, we introduced two possible photocatalytic mechanistic pathways, either through a type-II heterojunction or bioinspired Z-scheme charge dynamics. Under light illumination, the photocatalysts are excited and generate photoexcited e^-/h^+ pairs at their respective CB and VB positions. In the typical type-II charge migration mechanism, the photogenerated electron transfers from the CB TiO_2 to the lower potential CZUNH, and h^+ moves from the VB of CZUNH to TiO_2. However, the accumulated electrons on CZUNH restrict the formation of •OH radicals as the CB edge of CZUNH is measured as -0.24 eV, which is lower than the redox potential ($O_2/•O_2^- = -0.33$ eV). Thus, this result conflicts with the outcome of the radical scavenging experiments. Therefore, the conventional double charge transfer pathway was not suitable, but the bioinspired multivariate mediator-based Z-scheme is more appropriate for explaining the charge transfer mechanism that leads to the improved photocatalytic activity in the hybrid composite. Further, the Z-scheme charge transfer in the TiO_2/Ti_3C_2–TiC/CZUNH-20 heterostructure was validated by conducting terephthalic acid (TA) and nitrobluetetrazolium (NBT) tests. The synthesised photocatalyst was combined with 10 mL of NBT solution for the NBT test and subjected to 60 minutes of
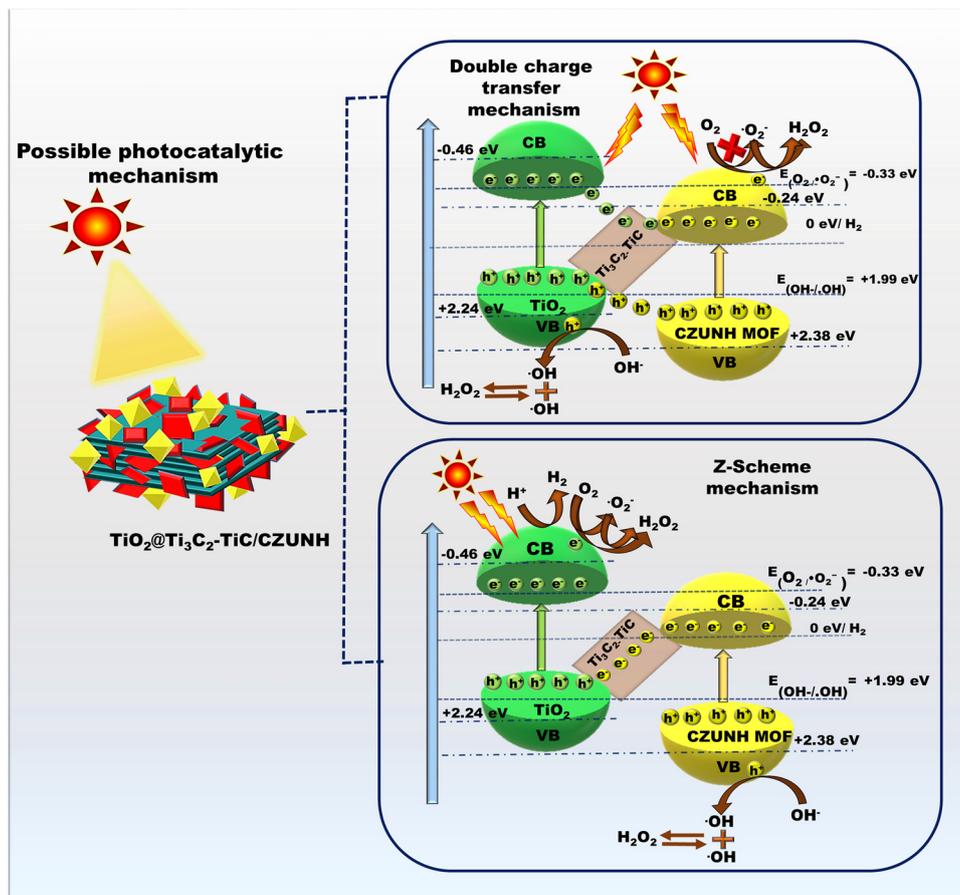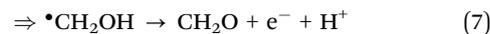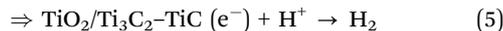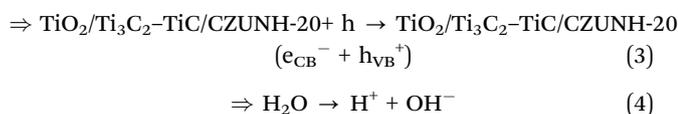

Scheme 2 Schematic representation of proposed photocatalytic mechanistic pathways for H_2O_2 and H_2 production.

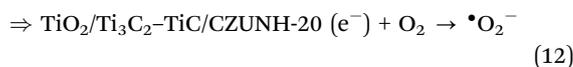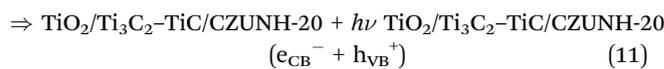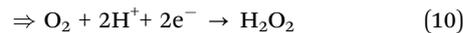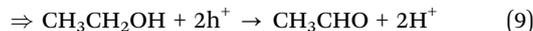solar exposure. After exposure, the sample was analysed by UV-vis spectroscopy, the decrease in NBT content shown in Fig. S8(a) (ESI†) proves that $^\bullet O_2^-$ radicals were generated during the photocatalysis process. Similar to this, the TA test was carried out to ascertain whether $^\bullet OH$ radicals were involved in the photocatalytic process. Equimolar terephthalic acid (TA) and 10 mL of the photocatalyst were mixed with NaOH solution for this experiment, and the mixture was exposed to solar light for 60 minutes. As illustrated in Fig. S8(b) (ESI†), an emission peak was seen in PL spectra, indicating the presence of $^\bullet OH$ radicals during the H_2O_2 production. This radical trapping experiment evidenced that the charge dynamics of the photogenerated charge carriers follow the Z-scheme pathway by forming $^\bullet O_2^-$ and $^\bullet OH$ radicals, which act as reactive species during the photocatalytic process. Under light illumination, electrons were excited from the VB to the CB in TiO_2 and CZUNH, while h^+ were generated in their respective VB. However, the Ti_3C_2 MXene possesses a lower Fermi level and higher metallic conductivity, causing the higher spatial charge separation at well-designed heterointerface regions. The electron migration in the interface regions of the multivariate mediator-based Z-scheme was validated by the XPS binding energy shifting. Due to the lower shifting of binding energy in TiO_2 ensued in increased donor density that confirmed the accumulation of electrons over the CB of TiO_2. Consequently, the photo-excited electrons of CZUNH were recombined with holes of TiO_2 via the solid-state electron mediator Ti_3C_2–TiC, enhancing the life span of electron and h^+ pairs in the CB_{TiO2} and VB_{CZUNH}. In the current scenario, Ti_3C_2–TiC acts as an intermediator for the higher flux electron transport bridge owing to its remarkable conductivity, which separated the photoinduced electrons and holes of TiO_2 and CZUNH at their respective CB and VB. In this way, effective charge carrier separation was accomplished, and the outcomes of the PL and Nyquist plot investigations support this representation. The scavenger test proved that the dominant species that were essential in the H_2O_2 generation were $^\bullet O_2^-$ and $^\bullet OH$ free radicals. The reserved electrons at the CB_{TiO2} have a band edge potential of -0.46 eV, satisfying the redox potentials of -0.33 V and $+0.69$ V for the consecutive dual-step one-electron $(O_2/^\bullet O_2^-/H_2O_2)$ indirect reduction and single-step dual-electron (O_2/H_2O_2) direct reduction pathways, respectively that can produce H_2O_2 upon light irradiation. h^+ at the VB_{CZUNH} have a band edge potential $+2.38$ eV, which is strong enough to generate $^\bullet OH$ radicals $(^\bullet OH/OH^- = +1.99$ eV), which combine with each other to produce H_2O_2. Additionally, the synthesized photocatalysts undergo a photocatalytic H_2 generation process using methanol as a hole scavenger. The photoexcited electron at the CB_{TiO2} reacts with the H^+ ion in water to produce H_2. Meanwhile, h^+ at the VB_{CZUNH} is consumed by the sacrificial agent. Combining all the processes, H_2O_2 and H_2 generation are illustrated in following equations:

Equation for H_2 production

$$\Rightarrow TiO_2/Ti_3C_2\text{–}TiC/CZUNH\text{-}20 + h \rightarrow TiO_2/Ti_3C_2\text{–}TiC/CZUNH\text{-}20 \; (e_{CB}^- + h_{VB}^+) \quad (3)$$

$$\Rightarrow H_2O \rightarrow H^+ + OH^- \quad (4)$$

$$\Rightarrow TiO_2/Ti_3C_2\text{–}TiC \; (e^-) + H^+ \rightarrow H_2 \quad (5)$$

$$\Rightarrow CH_3OH + h^+ \rightarrow {}^\bullet CH_2OH + H^+ \quad (6)$$

$$\Rightarrow {}^\bullet CH_2OH \rightarrow CH_2O + e^- + H^+ \quad (7)$$

$$\Rightarrow H^+ + e^- \rightarrow H_2 \quad (8)$$

Equation for H_2O_2 production

$$\Rightarrow CH_3CH_2OH + 2h^+ \rightarrow CH_3CHO + 2H^+ \quad (9)$$

$$\Rightarrow O_2 + 2H^+ + 2e^- \rightarrow H_2O_2 \quad (10)$$

$$\Rightarrow TiO_2/Ti_3C_2\text{–}TiC/CZUNH\text{-}20 + h\nu \; TiO_2/Ti_3C_2\text{–}TiC/CZUNH\text{-}20 \; (e_{CB}^- + h_{VB}^+) \quad (11)$$

$$\Rightarrow TiO_2/Ti_3C_2\text{–}TiC/CZUNH\text{-}20 \; (e^-) + O_2 \rightarrow {}^\bullet O_2^- \quad (12)$$

$$\Rightarrow TiO_2/Ti_3C_2\text{–}TiC/CZUNH\text{-}20 \; (e^-) + {}^\bullet O_2^- + 2H^+ + 2e^- \rightarrow H_2O_2 \quad (13)$$

$$\Rightarrow TiO_2/Ti_3C_2\text{–}TiC/CZUNH\text{-}20 \; (h^+) + 2OH^- \rightarrow 2{}^\bullet OH \quad (14)$$

$$\Rightarrow {}^\bullet OH + {}^\bullet OH \rightarrow H_2{}^\bullet O_2 \quad (15)$$
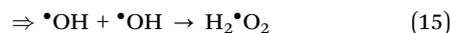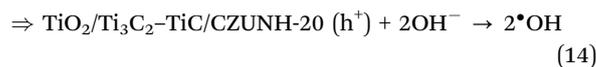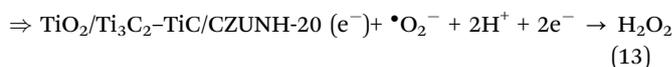
5. Conclusion

In summary, the current work illustrates a high-throughput interfacial engineering strategy for constructing a multicomponent TiO_2/Ti_3C_2–TiC/CZUNH composite with a Z-scheme charge transfer pathway by a two-step hydrothermal approach for photocatalytic H_2O_2 and H_2 generation. Here, layered Ti_3C_2–TiC was employed as a precursor to obtain TiO_2 nanosheets and used as a solid-state high-flux electron bridge to realize quick charge transfer and separation. The designed strategy includes the in situ growth of TiO_2 nanosheets across the edges of a 2D Ti_3C_2–TiC layer, and CZUNH was distributed on the TiO_2/Ti_3C_2–TiC hybrid. The TiO_2/Ti_3C_2–TiC/CZUNH heterostructure hybrid with CZUNH content of 20% achieved a significantly enhanced H_2O_2 yield of 1575 µmol h^{-1} g^{-1}, which is approximately 3.5- and 2.8-fold higher than those of neat TiO_2/Ti_3C_2–TiC and CZUNH respectively. Moreover, the visible light H_2 evolution rate reached 570 µmol h^{-1}, which is four and three times higher than the rates of respective neat TiO_2/Ti_3C_2–TiC and CZUNH. The elevated photocatalytic performance and stability of the hybrid material were ascribed to enhanced light absorption capacity, large active surface area and rapid charge separation. This output was proved by a lower Nyquist plot, shifts in band edge potential, higher surface area, lower PL intensity, and enhanced TRPL life span. The determined mechanistic pathway followed a Z-scheme of higher flux electron transport channelizer charge dynamics due to the higher metallic conductivity of MXene. This work offers a new perspective for the design and regulation of the interface heterostructure for multivariate solid-state Z-scheme MXene-derived

heterojunctions and thoroughly interprets interfacial electronic state modulation to enhance photocatalytic performance.

Conflicts of interest

There are no conflicts to declare.

Acknowledgements

References

1 S. Chu and A. Majumdar, *Nature*, 2012, **488**, 294–303.

2 P. Lian, Y. Dong, Z. S. Wu, S. Zheng, X. Wang, S. Wang, C. Sun, J. Qin, X. Shi and X. Bao, *Nano Energy*, 2017, **40**, 1–8.

3 W. Zhao, P. Yan, B. Li, M. Bahri, L. Liu, X. Zhou, R. Clowes, N. D. Browning, Y. Wu, J. W. Ward and A. I. Cooper, *J. Am. Chem. Soc.*, 2022, **144**, 9902–9909.

4 L. Wang, J. Zhang, Y. Zhang, H. Yu, Y. Qu and J. Yu, *Small*, 2022, **18**, 2104561.

5 S. Mansingh, D. P. Sahoo, L. Paramanik, M. Sahoo and K. Parida, *Inorg. Chem. Front.*, 2022, **9**, 559–576.

6 L. Acharya, G. Swain, B. P. Mishra, R. Acharya and K. Parida, *ACS Appl. Energy Mater.*, 2022, **5**, 2838–2852.

7 B. P. Mishra, L. Biswal, S. Das, L. Acharya and K. Parida, *Langmuir*, 2023, **39**, 957–971.

8 K. K. Das, S. Mansingh, R. Mohanty, D. P. Sahoo, N. Priyadarshini and K. Parida, *J. Phys. Chem. C*, 2022, **127**, 22–40.

9 F. Sandelin, P. Oinas, T. Salmi, J. Paloniemi and H. Haario, *Ind. Eng. Chem. Res.*, 2006, **45**, 986–992.

10 C. M. Crombie, R. J. Lewis, R. L. Taylor, D. J. Morgan, T. E. Davies, A. Folli, D. M. Murphy, J. K. Edwards, J. Qi, H. Jiang, C. J. Kiely, X. Liu, M. S. Skjøth-Rasmussen and G. J. Hutchings, *ACS Catal.*, 2021, **11**, 2701–2714.

11 H. Hou, X. Zeng and X. Zhang, *Angew. Chem., Int. Ed.*, 2020, **59**, 17356–17376.

12 J. K. Edwards, E. Ntainjua N, A. F. Carley, A. A. Herzing, C. J. Kiely and G. J. Hutchings, *Angew. Chem., Int. Ed.*, 2009, **48**, 8512–8515.

13 L. Chen, C. Chen, Z. Yang, S. Li, C. Chu and B. Chen, *Adv. Funct. Mater.*, 2021, **31**, 2105731.

14 X. Huang, W. Liu, J. Zhang, M. Song, C. Zhang, J. Li, J. Zhang and D. Wang, *ACS Appl. Mater. Interfaces*, 2022, **14**, 11350–11358.

15 A. Fujishima and K. Honda, *Nature*, 1972, **238**, 37–38.

16 M. Ni, M. K. Leung, D. Y. Leung and K. Sumathy, *Renewable Sustainable Energy Rev.*, 2007, **11**, 401–425.

17 S. Pany, B. Naik, S. Martha and K. Parida, *ACS Appl. Mater. Interfaces*, 2014, **6**, 839–846.

18 S. Pany and K. Parida, *ACS Sustainable Chem. Eng.*, 2014, **2**, 1429–1438.

19 L. Zheng, H. Su, J. Zhang, L. S. Walekar, H. V. Molamahmood, B. Zhou, M. Long and Y. H. Hu, *Appl. Catal., B*, 2018, **239**, 475–484.

20 M. Naguib, M. Kurtoglu, V. Presser, J. Lu, J. Niu, M. Heon, L. Hultman, Y. Gogotsi and M. W. Barsoum, *Adv. Mater.*, 2011, **23**, 4248–4253.

21 B. Anasori, M. R. Lukatskaya and Y. Gogotsi, *Nat. Rev. Mater.*, 2017, **2**, 16098.

22 A. Nashim and K. Parida, *Sustainable Mater. Technol.*, 2022, **32**, e00439.

23 K. Huang, C. Li, H. Li, G. Ren, L. Wang, W. Wang and X. Meng, *ACS Appl. Nano Mater.*, 2020, **3**, 9581–9603.

24 L. Biswal, S. Nayak and K. Parida, *Catal. Sci. Technol.*, 2021, **11**, 1222–1248.

25 A. Sherryna and M. Tahir, *ACS Appl. Energy Mater.*, 2021, **4**, 11982–12006.

26 L. Biswal, R. Mohanty, S. Nayak and K. Parida, *J. Environ. Chem. Eng.*, 2022, **10**, 107211.

27 Z. You, Y. Liao, X. Li, J. Fan and Q. Xiang, *Nanoscale*, 2021, **13**, 9463–9504.

28 T. Su, Z. D. Hood, M. Naguib, L. Bai, S. Luo, C. M. Rouleau, I. N. Ivanov, H. Ji, Z. Qin and Z. Wu, *ACS Appl. Energy Mater.*, 2019, **2**, 4640–4651.

29 Y. Zhou, M. Yu, R. Zhan, X. Wang, G. Peng and J. Niu, *Sep. Purif. Technol.*, 2021, **275**, 119194.

30 J.-Y. Li, Y.-H. Li, F. Zhang, Z.-R. Tang and Y.-J. Xu, *Appl. Catal., B*, 2020, **269**, 118783.

31 K. Wang, X. Li, N. Wang, Q. Shen, M. Liu, J. Zhou and N. Z. Li, *Ind. Eng. Chem. Res.*, 2021, **60**, 8720–8732.

32 L. Biswal, B. P. Mishra, S. Das, L. Acharya, S. Nayak and K. Parida, *Inorg. Chem.*, 2023, **62**, 7584–7597.

33 L. Biswal, L. Acharya, B. P. Mishra, S. Das, G. Swain and K. Parida, *ACS Appl. Energy Mater.*, 2023, **6**, 2081–2096.

34 C. Peng, P. Wei, X. Li, Y. Liu, Y. Cao, H. Wang, H. Yu, F. Peng, L. Zhang, B. Zhang and K. Lv, *Nano Energy*, 2018, **53**, 97–107.

35 H. Liu, C. Yang, X. Jin, J. Zhong and J. Li, *Colloids Surf., A*, 2020, **603**, 125239.

36 M. Tahir, *Energy Fuels*, 2021, **35**, 14197–14211.

37 X. Qin, R. Cao, W. Gong, L. Luo, G. Shi, L. Ji and A. Zhu, *J. Solid State Chem.*, 2022, **306**, 122750.

38 Y. Liu, Y.-H. Li, X. Li, Q. Zhang, H. Yu, X. Peng and F. Peng, *ACS Nano*, 2020, **14**, 14181–14189.

39 P. Wei, Y. Chen, T. Zhou, Z. Wang, Y. Zhang, H. Wang, H. Yu, J. Jia, K. Zhang and C. Peng, *ACS Catal.*, 2022, **13**, 587–600.

40 S. Subudhi, D. Rath and K. M. Parida, *Catal. Sci. Technol.*, 2018, **8**, 679–696.

41 S. P. Tripathy, S. Subudhi and K. Parida, *Coord. Chem. Rev.*, 2021, **434**, 213786.

42 S. Subudhi, S. P. Tripathy and K. Parida, *Inorg. Chem. Front.*, 2021, **8**, 1619–1636.

43 Y. Fan, H. Zhang, M. Ren, Y. Zhang, Y. Li, L. Wang and J. Chen, *Chem. Eng. J.*, 2021, **414**, 128782.

44 A. Loosen, C. Simms, S. Smolders, D. E. De Vos and T. N. Parac-Vogt, *ACS Appl. Nano Mater.*, 2021, **4**, 5748–5757.

45 X.-D. Du, X.-H. Yi, P. Wang, W. Zheng, J. Deng and C.-C. Wang, *Chem. Eng. J.*, 2019, **356**, 393–399.

46 J. Tan, X. He, F. Yin, X. Liang and G. Li, *Int. J. Hydrogen Energy*, 2021, **46**, 31647–31658.

47 A. Lin, A. A. Ibrahim, P. Arab, H. M. El-Kaderi and M. S. El-Shall, *ACS Appl. Mater. Interfaces*, 2017, **9**, 17961–17968.

48 J. He, Y. Xu, W. Wang, B. Hu, Z. Wang, X. Yang, Y. Wang and L. Yang, *Chem. Eng. J.*, 2020, **379**, 122431.

49 X.-P. Wu, L. Gagliardi and D. G. Truhlar, *J. Am. Chem. Soc.*, 2018, **140**, 7904–7912.

50 C. Gomes Silva, I. Luz, F. X. Llabrés i Xamena, A. Corma and H. García, *Chem. – Eur. J.*, 2010, **16**, 11133–11138.

51 L. Shen, S. Liang, W. Wu, R. Liang and L. Wu, *Dalton Trans.*, 2013, **42**, 13649–13657.

52 S. P. Tripathy, S. Subudhi, A. Ray, P. Behera, G. Swain, M. Chakraborty and K. Parida, *Langmuir*, 2023, **39**, 7294–7306.

53 S. P. Tripathy, S. Subudhi, A. Ray, P. Behera, J. Panda, S. Dash and K. Parida, *J. Colloid Interface Sci.*, 2023, **629**, 705–718.

54 L. Biswal, S. Nayak and K. Parida, *J. Colloid Interface Sci.*, 2022, **621**, 254–266.

55 L. Jin, H. Liu, A. Xu, Y. Wu, J. Lu, J. Liu, S. Xie, Y. Yao, L. Dong, M. Zhang and S. Kai, *Microporous Mesoporous Mater.*, 2021, **317**, 110997.

56 S. Ren, J. Dong, X. Duan, T. Cao, H. Yu, Y. Lu and D. Zhou, *J. Chem. Eng.*, 2023, **460**, 141884.

57 S. Li, H. Li, Y. Wang, Q. Liang, M. Zhou, D. Guo and Z. Li, *Sep. Purif. Technol.*, 2024, **333**, 125994.

58 S. Zhao, S. Li, Y. Long, X. Shen, Z. Zhao, Q. Wei, S. Wang, Z. Zhang, X. Zhang and Z. Zhang, *Chemosphere*, 2021, **280**, 130637.

59 S. Mansingh, S. Subudhi, S. Sultana, G. Swain and K. Parida, *ACS Appl. Nano Mater.*, 2021, **4**, 9635–9652.

60 H. Peng, L. Wang, Y. Zhou, B. Li, X. Zheng and J. Wen, *Microporous Mesoporous Mater.*, 2024, **365**, 112894.

61 M. Cabrero-Antonino, A. Melillo, E. Montero-Lanzuela, M. Álvaro, B. Ferrer, I. Vaya, H. G. Baldoví and S. Navalón, *J. Chem. Eng.*, 2023, **468**, 143553.

62 E. Geravand, F. Farzaneh, R. Gil-San-Millan, F. J. Carmona and J. A. Navarro, *Inorg. Chem.*, 2020, **59**, 16160–16167.

63 X. Zhang, S. Tong, D. Huang, Z. Liu, B. Shao, Q. Liang, T. Wu, Y. Pan, J. Huang, Y. Liu and M. Cheng, *Chem. Rev.*, 2021, **448**, 214177.

64 H. Mohebali, G. Moussavi, M. Karimi and S. Giannakis, *Sep. Purif. Technol.*, 2023, **315**, 123670.

65 L. M. Valdivieso Zarate, C. A. Bravo Sanabria, G. E. Ramírez Caballero and F. Martínez Ortega, *Eur. J. Inorg. Chem.*, 2023, 202300194.